PAPER

Check for updates

Investigation of the role of in-plane stress behavior on ferroelectric properties of scaled-up hafnium zirconium oxide superlattices†

Gourab De, [ID] *[a,c] Mihaela Ioana Popovici,[c] Shankha Mukherjee,[a,c] Dae Seon Kwon,[c,d] Federica Luciano,[b,c] Tony Murphy,[c] Gouri Sankar Kar,[c] Annelies Delabie[b,c] and Jan Van Houdt[a,c]

Hafnium zirconium oxide (HZO) based ferroelectric (FE) devices are promising candidates for next-generation low-power memory applications. Recently, there has been a growing interest in implementing HZO-based superlattice structures to improve FE response, resonator applications, and for physical analysis needed for in-depth understanding of scaled-down HZO, as it is challenging to characterize sub-10 nanometer-thin films. However, it has not been explored whether these superlattices retain identical FE properties as they are scaled up. In this work, we have looked into the role of in-plane stress on FE properties of superlattices, by designing superlattices that consist of different numbers of alternating layers of atomic layer deposited 9 nm thick lanthanum doped HZO (La:HZO) and 0.5 nm thick Al_2O_3 interlayers, sandwiched between a top and bottom electrode (TE and BE). Here we show that after annealing the stacks, for a given BE/TE, in-plane stress becomes independent of the number of HZO layer repeats in the superlattice, thereby retaining a similar FE/non-FE phase composition, which results in an identical FE response. Discrepancies in FE properties between the single-layer HZO stack and the superlattices are attributed to differences in phase composition, emphasizing the impact of in-plane stress and interfaces. Therefore, this suggests that it is possible to scale up these superlattices while preserving identical FE properties by tuning the in-plane stress of the HZO layers and their interfaces, making them suitable for characterization purposes and applications that require thicker FE HZO films.

Introduction

Since the accidental discovery of ferroelectricity in doped hafnium oxide in 2011,[1] hafnium oxide-based ferroelectric (FE) materials have been the choice for emerging FERAM technologies.[2–4] Unlike FE perovskites, hafnium oxide and its other variants can be deposited by atomic layer deposition (ALD) and are complementary metal oxide semiconductor (CMOS) and back-end of line (BEOL) compatible.[4] Moreover, when scaling down to a thinner layer for low voltage memory operations, they exhibit a better FE response.[5] This is because in hafnia-based oxides ferroelectricity is shown by primarily one crystallographic phase, *i.e.* the non-centrosymmetric $Pca2_1$

orthorhombic III phase (o-phase), which is metastable in nature.[6] Thin films of these fluorite-structured oxides are polymorphic in nature, *i.e.* a mixture of different phases exist at the same time: antiferroelectric tetragonal (t-phase), non-FE monoclinic (m-phase) and cubic phases, and o-phases.[7–10] The stability of this specific FE o-phase is dependent on oxygen vacancy concentration, strain, and grain size, with tensile strain and smaller grain size having a favorable effect in stabilizing the o-phase.[11–13] It has been recently reported[14] that the FE o-phase can be stabilized in films with large grain sizes, but this was observed for epitaxial HZO films, where o-phase stabilization is likely due to epitaxial strain and a higher degree of structural order across the film. Since ALD deposited HZO films are polycrystalline, such stabilization effects are not possible here. So, to stabilize o-phase in such ALD-based thin films, thinner layers are deposited which result in smaller grain size.[11,15]

However, accurately identifying different crystallographic phases in hafnium oxide-based thin films below 10 nm poses a significant challenge. One of the commonly used techniques is grazing-incidence X-ray diffraction (GI-XRD). Although it can successfully distinguish the m-phase from the o- & t-phase, differentiating between the o- and t-phase is not possible

[a]Department of Physics & Astronomy, KU Leuven, Leuven, Belgium.
E-mail: gourab.de@imec.be
[b]Department of Chemistry, KU Leuven, Leuven, Belgium
[c]imec, Leuven, Belgium
[d]Department of Chemical and Biological Engineering, Sookmyung Women's University, Seoul, Republic of Korea
†Electronic supplementary information (ESI) available. See DOI: https://doi.org/10.1039/d4nr05053c

because of their similar 2θ angle position. In the past, researchers have explored various alternative methods for characterizing crystalline phases beyond the commonly used X-ray diffraction (XRD).[16–19] While methods like precession electron diffraction (PED)[18] and extended X-ray absorption fine-structure spectroscopy (EXAFS)[16] can distinguish between the o- and t-phases, these techniques are limited in scan area and often require complex synchrotron facilities. However, recently, the work of Schroeder et al.[19] has highlighted the capability of Raman spectroscopy in differentiating the o- and t- phases, a technique that is non-destructive in nature. However, to get a sufficiently strong Raman signal, a 30 nm thick superlattice based on alternating layers of $Hf_{1-x}Zr_xO_2$ was required. Similarly, other characterization techniques like nano-indentation for determining elastic parameters or residual stress from suspended cantilevers require even thicker films.[20–22] Apart from addressing characterization challenges, many applications require thick FE films like for micro or nano-electromechanical systems (MEMS/NEMS) as pyroelectric infrared sensors or as resonators for high-frequency applications.[23,24]

Consequently, it is pertinent to inquire whether these superlattices preserve the properties of the single-layer FE film they aim to replicate. In literature, the most common superlattice structure for HZO has been alternating layers of HZO separated by an ultra-thin Al_2O_3 interlayer.[19,22,24–26] The role of the Al_2O_3 interlayers is to prevent grain growth in the vertical direction, thereby preventing the formation of non-FE m-phase.[26] Here in our work, superlattices consisting of multiple repeats of 9 nm lanthanum doped stoichiometric HZO (La:HZO) layers separated by 0.5 nm Al_2O_3 interlayers were fabricated. La-dopant has been widely reported to suppress non-FE m-phase formation,[7,27,28] which should further help to suppress m-phase formation along with grain confinement. We have specifically focused on the role of in-plane stress in determining the FE properties, as it has been rarely studied for HZO superlattices. As grain size is already confined for all the superlattices, factors like in-plane stress and oxygen vacancy distribution will play a role in determining the FE/non-FE composition. Oxygen vacancies are very difficult to characterize, but being defects, they likely influence the strain in a given layer.[29,30] So, by studying the stress behavior, some knowledge regarding the oxygen vacancy distribution can be inferred.

We have employed transmission electron microscopy (TEM) and energy-dispersive X-ray spectroscopy (EDS) to assess the stability of the Al_2O_3 interlayer following post-metallization annealing (PMA). In-plane stress behavior and crystallinity of these stacks have been studied using wafer curvature measurements and grazing incident X-ray diffraction (GIXRD). Positive-Up Negative-Down (PUND) pulsing scheme, and endurance measurements were conducted to study the FE response of these stacks. These techniques were utilized to check whether these superlattices retained their FE properties as they were scaled up and whether they replicated the FE properties of an individual La:HZO layer.

Experimental

Fabrication

The fabrication process is shown in Fig. 1(b). Thermal atomic layer deposition (ALD) has been used to deposit all layers in the metal-FE-metal stacks on 775 µm p-doped silicon 300 mm diameter wafers. 10 nm titanium nitride (TiN) grown at 360 °C by ALD was employed as top and bottom metal electrodes (TE and BE, respectively). The superlattices consisting of 9 nm $Hf_{0.5}Zr_{0.5}O_2$ with 1.8 at% La doping (La:HZO) and 0.5 nm Al_2O_3 layers were deposited at 300 °C in an alternating manner with 3 up to 6 repeats according to the envisaged thickness (Fig. 1(a)). A single 9 nm La:HZO was used as a reference. After deposition of the TiN TE, the stacks were subjected to post-metallization annealing (PMA) at a temperature of 550 °C, in N_2 atmosphere, for 60 s to complete the crystallization of the HZO layers. Since TiN TE were only 10 nm thick, probing for electrical measurements was difficult. So, these TiN TE were etched away using a solution of NH_4OH, H_2O_2 and deionized water in 1 : 4 : 20 ratio at 65 °C, and 70 nm thick circular platinum (Pt) electrodes (120 µm diameter) were deposited on top of the HZO layer to conduct electrical characterization of the stacks (Fig. 1(a)).

Material & electrical characterization

The crystallinity of the HZO superlattices was confirmed using GI-XRD with Cu Kα X-rays with λ = 1.54056 Å, incidence angle (ω) = 0.5° and scanned with a 2θ range of 20–65°. Peak posi-
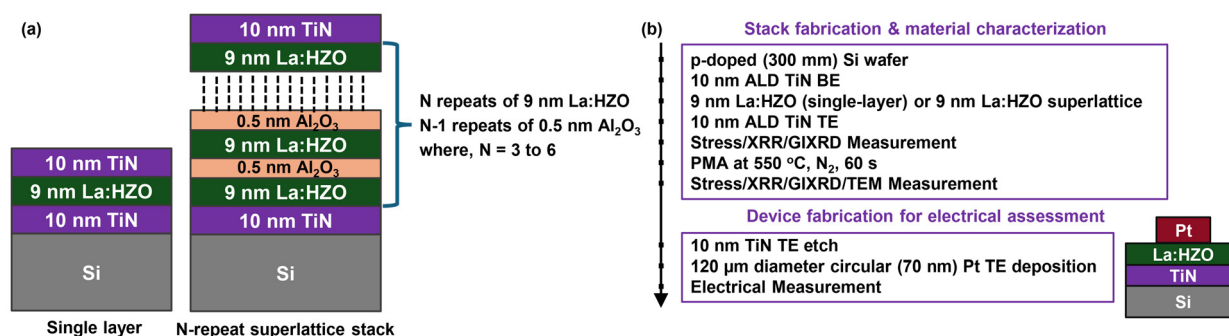

Fig. 1 (a) Schematic diagram of single layer and superlattice La:HZO stacks, (b) flow for FE stack/device fabrication/characterization.

tions were estimated using Pseudo-Voigt fitting. The thickness of the superlattice stacks was calculated from X-ray reflectivity (XRR) measurements (scan step size: 40 s, scan range: 15 600 s). The stress of the superlattice stacks was evaluated using wafer curvature measurements performed by spectroscopic ellipsometry from 69 points on each wafer, where the elastic parameters of the silicon wafer (Young's modulus = 127 GPa, Poisson' ratio = 0.278) were employed. Cross-sectional TEM, dark-field scanning transmission electron microscopy (DF-STEM) & EDS were performed at 200 kV. Electrical measurements were performed on 120 μm diameter devices by biasing the bottom electrode through the Si wafer and connecting the top Pt electrode to the ground. Endurance measurements were carried out at 4 MV cm^{-1} by cycling the devices using a bipolar trapezoidal pulse at 16.67 kHz while positive-up-negative-down or PUND measurements were carried out in between to measure the FE polarization. The pulsing scheme is shown in Fig. 5(a).

Results & discussion

Superlattice stack description

Fig. 1(a) shows the stack structure for the superlattices where 9 nm La:HZO layers were repeated multiple times, separated by 0.5 nm thin Al_2O_3 interlayers. Four stacks with 3, 4, 5, and 6 repeats of 9 nm La:HZO layer were studied, while keeping the same bottom and top electrodes. Subsequently, the stacks were subjected to PMA to enhance the crystallinity of the HZO layer, thereby allowing the formation of o-phase. Following PMA, the HZO superlattices with 3,4,5,6-repeat show a total thickness of 28 nm, 39 nm, 49 nm and 58 nm respectively based on X-ray reflectivity (XRR) analysis (Fig. S1†). Fig. 2(a) shows the cross-sectional TEM of 6-repeat La:HZO superlattice stack. The superlattice thickness is around 59 nm, which matches the value extracted from XRR (58 nm). Each individual HZO layer (around 9.4 nm thick) can be clearly distinguished from the cross-sectional TEM & DF-STEM image (Fig. 2(a) and (b)), showing that the Al_2O_3 interlayer remains stable even after the stack has been subjected to annealing

(PMA). Energy dispersive spectroscopy (EDS) confirms the stability of the Al_2O_3 interlayer as shown in Fig. 2(c), where no significant interdiffusion of aluminium is observed into the adjacent HZO layers. The stability of Al_2O_3 interlayers is vital, as it helps in confining the HZO grain size in the vertical direction to 9 nm as one would expect in a FE stack with a single 9 nm thick HZO layer. Ideally, this should help suppress the formation of the non-FE m-phase.

Understanding stress behavior and crystallinity

As stated a priori, crystallographic phase stability in HZO is widely believed to be influenced by the in-plane stress in the film. Multiple studies have reported that tensile in-plane stress should promote the formation of FE o-phase.[12,28,31] Therefore, to better understand the impact of increasing the number of HZO layer repeats, in-plane stress behavior was studied. Fig. 3(a) shows the in-plane stress behavior of the full stack (BE + HZO + TE) prior to annealing the superlattice. The total in-plane stack stress is observed to be tensile and becomes even more tensile with increasing total superlattice thickness (or number of La:HZO layer repeats). GI-XRD patterns (Fig. 2(b)) of the as-deposited superlattices show strong o(111)/t(101) reflection, indicating these layers are already crystallized, unlike the single-layer 9 nm La:HZO reference. Considering that the HZO grain sizes in the vertical direction were almost identical for each sample since the HZO layers were clearly separated by the Al_2O_3 interlayers, the XRD signals from the superlattice would represent the accumulated contributions from multiple unit 9 nm-thick HZO layers. Furthermore, the XRD peaks near 2θ of ~30.5° from the superlattices showed quite asymmetric shapes, suggesting a higher fraction of the t-phase compared to the o-phase in the HZO. This is consistent with the t(101) peak (~30.6°) appearing at a slightly higher angle than the o(111) peak (~30.3°).[7–10,27] A shift of the o(111)/t(101) peaks toward a higher angle with the increasing number of repeats of HZO layers (increasing total superlattice thickness) is also observed, suggesting possibly the increase of t-phase in with superlattice thickness. These results suggest that in as-deposited condition, the superlattices show weak crystallinity with tetragonal-rich phase compo-
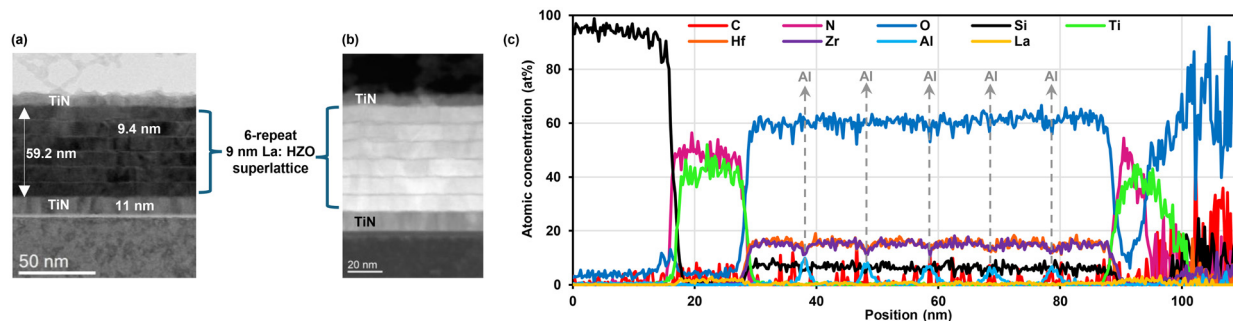
Fig. 2 (a) Cross-sectional TEM of 6-repeat La:HZO superlattice, (b) dark-field STEM (DF-STEM) of the 6-repeat La:HZO superlattice showing clearly the separation of the individual La:HZO layers, (c) EDS spectrum of the 6-repeat La:HZO superlattice. The dashed lines in the EDS spectrum highlight the location of the aluminium signals.
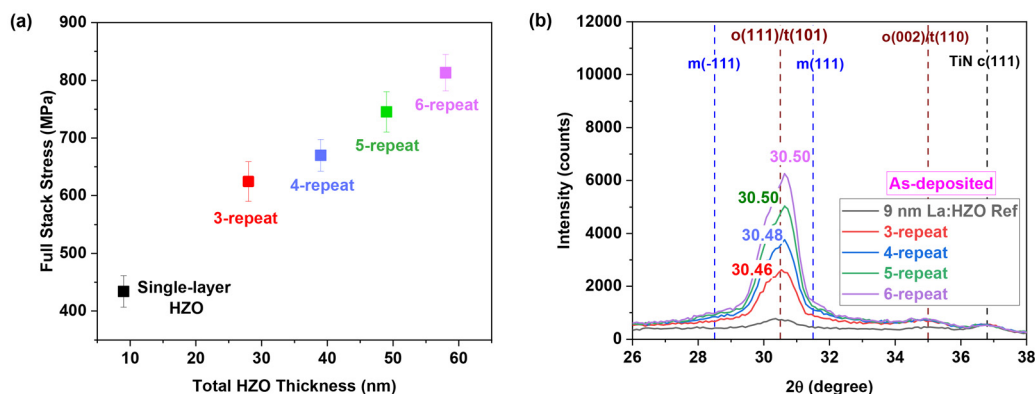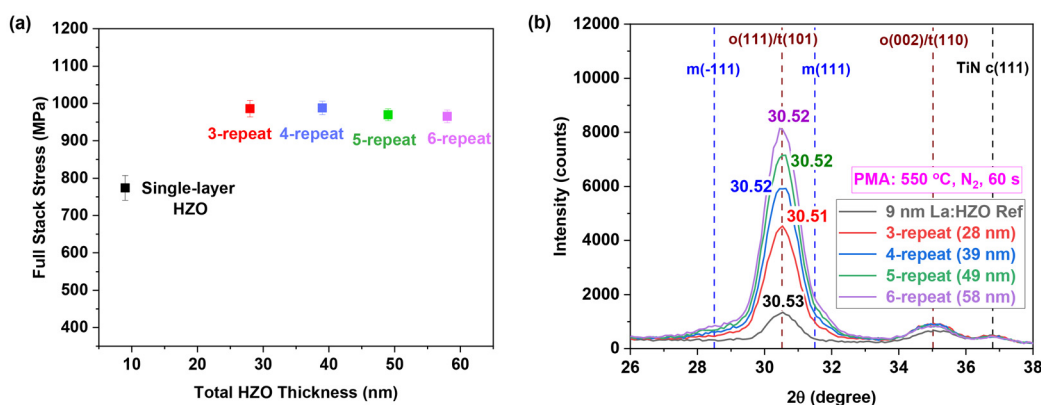
Fig. 3 (a) Full stack stress of single-layer La:HZO reference and La:HZO superlattices of different total thicknesses under as-deposited condition (with TE), (b) GI-XRD of single-layer La:HZO and La:HZO superlattices as-deposited. The dashed vertical lines indicate the expected peak positions for the o, t, and m crystallographic phases of HZO and cubic [c] phase of TiN electrodes. The numbers on the peaks correspond to the peak position, which was extracted from Pseudo-Voigt function data fitting. Here the BE and TE are the same 10 nm TiN.

sition. The reason for the in-plane stress becoming more tensile with the increasing number of repeats is likely due to the stacks becoming more crystalline. With increasing repeats in the superlattices, as the deposition process is longer, the already deposited HZO layers are subjected to a higher thermal budget (longer duration at the deposition temperature of 300 °C) in stacks with a higher number of repeats. This results in "*in situ* annealing" of the already deposited HZO layers, enhancing their crystallinity, and thereby making the in-plane stack stress more tensile in nature.

However, upon annealing the entire superlattice stacks, which results in complete crystallization of the HZO layers, significant change is observed in both in-plane stress behavior and crystallinity from GI-XRD (Fig. 4). In-plane stress becomes independent of the total superlattice thickness (or the number of HZO layer repeats) (Fig. 4(a)) and the peak position of o(111)/t(101) crystallite is almost the same (around 30.52°) for

all the superlattices of different thicknesses (Fig. 4(b)). Since the BE and TE are the same for all the superlattices, this suggests that after annealing, all the superlattices of different HZO layer repeats have essentially the same intrinsic stress. As crystallographic phase stability is influenced by in-plane stress in HZO, for similar grain/crystallite size, identical in-plane stress should result in identical phase composition in the different superlattices. This is supported by GIXRD spectra, which show similar o(111)/t(101) crystallite peak positions across the superlattices, with symmetrical peak shapes, indicating that they have identical phase compositions and henceforth should show similar values of remanent polarization. Only a slight difference in the o(111)/t(101) peak position is observed for the 3-repeat superlattice (30.51° *vs.* 30.52° for the rest), which when considering the error in Pseudo-Voigt fit of 0.005°, this difference in peak position is within the error range (after considering rounding up to the second decimal digit).

Fig. 4 (a) Full stack stress of single-layer La:HZO reference and La:HZO superlattices of different total thicknesses after PMA, (b) GI-XRD of single-layer La:HZO and La:HZO superlattices post-PMA (thickness of the superlattices in brackets). The dashed vertical lines indicate the expected peak positions for the o, t, and m crystallographic phases of HZO and cubic [c] phase of TiN electrodes. The numbers on the peaks correspond to the peak position, which was extracted from Pseudo-Voigt fitting. Here the BE and TE are the same 10 nm TiN.

Electrical evaluation & further discussion

To verify the understanding from material characterization and to evaluate the electrical properties, pulse measurements are carried out using the waveforms as shown in Fig. 5(a). Fig. 5(b) shows the endurance behavior of the superlattices, and Fig. 5(c and d) shows the P–E loops at pristine state and after 10^4 cycles, respectively. As expected from the material properties, the pristine $2P_r$ for the superlattices of various thicknesses/HZO layer repeats are identical (around 9–10 μC cm^{-2}) and cycling behavior is quite similar up to 10^2 cycles, after which a slight drift in $2P_r$ values has been observed. This essentially confirms that despite increasing the number of HZO layer repeats, preservation of in-plane stress has resulted in almost identical FE/non-FE phase composition, leading to similar FE characteristics. This shows that HZO superlattices can be scaled up while preserving identical FE properties under pristine state, making them suitable for characterization purposes.

The Al$_2$O$_3$ interlayers here play a critical role in the preservation of FE properties across the superlattices. From the TEM and DF-STEM shown in Fig. 2(a) and (b) respectively, the Al$_2$O$_3$ layer is amorphous in nature and from XRR are estimated to be around 0.5 nm thick. Since the Al$_2$O$_3$ layer acts as the substrate for the to-be-deposited HZO layer on top, it influences factors like nucleation, grain growth, and grain coalescence, which stress development in the HZO layer. The Al$_2$O$_3$ layer can also affect defect densities (oxygen vacancies) in the HZO layer, which likely has some impact on in-plane stress.[29,30] Since the Al$_2$O$_3$ layers are amorphous and have the same thickness for all superlattices, they lead to the development of similar in-plane stress and likely similar oxygen vacancy distri-

bution in each of the HZO layers in the superlattices. This likely results in identical FE/non-FE phase composition across the superlattices as suggested by comparable 2θ peak values (from Pseudo Voigt fit) corresponding to o(111)/t(101) and FE response (Fig. 5(b)), at least up to 10^2 cycles. After 10^2 cycles, re-distribution of oxygen vacancies likely occurs, due to oxygen scavenging by TiN electrodes. So, the oxygen vacancy distribution in the HZO layers in the middle of the superlattices likely no longer remains similar, leading to the observed drift in FE response beyond 10^2 cycles.

Fig. 5(c) and (d) show that the P–E loops are similar across all the superlattices, indicating that for the same applied electric field, the polarization/FE-response of the superlattices is comparable. This points towards Al$_2$O$_3$ layers preventing interlayer polarization coupling between the FE layers. This is an unexpected observation, as superlattices constructed of alternating layers of different perovskite-based FE materials often show cooperative polarization or anti-polarization due to this coupling effect.[32,33] This results in the strengthening or weakening of the polarization across the stack. In our case, the superlattice is constructed of alternating FE and dielectric layers, as opposed to both being FE; where the Al$_2$O$_3$ layer likely acts as an 'isolator', preventing interlayer FE coupling. In future studies, we plan to look into the role of the Al$_2$O$_3$ layer in blocking this interlayer coupling.

Although the superlattices show quite similar FE responses when compared to each other, a quite remarkable difference is observed between the superlattices and the single-layer La: HZO stack, which shows considerably higher polarization values. It can be observed from Fig. 3(a), that in comparison to the single layer 9 nm La:HZO, the superlattices have an increased signal of m-phase with a predominant m(111) and
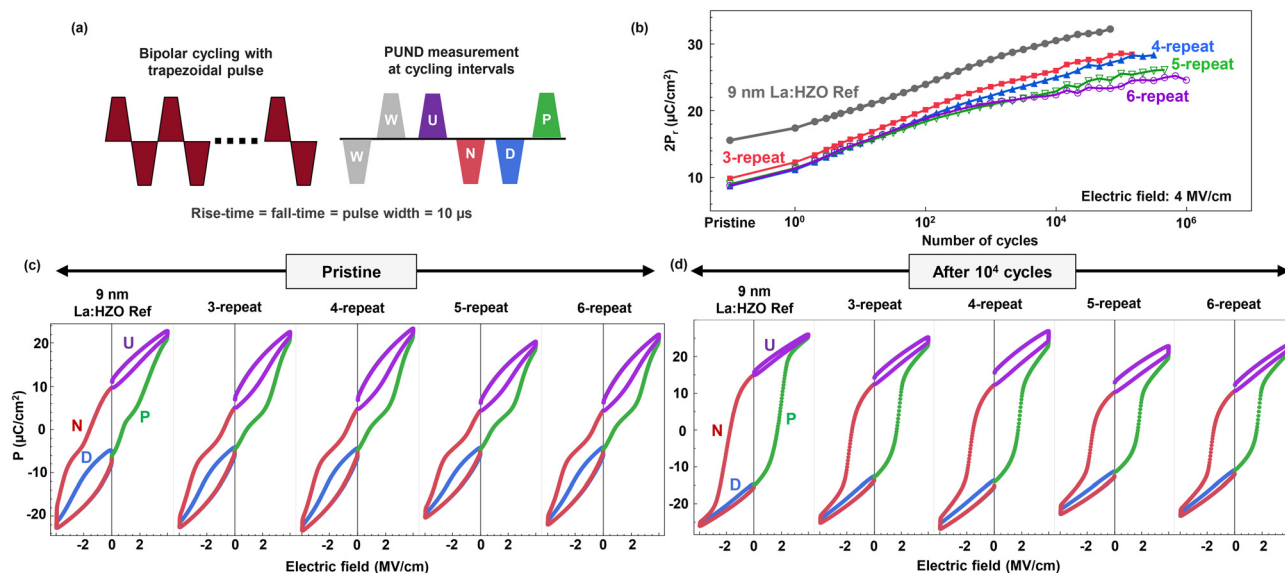
Fig. 5 (a) Bipolar trapezoidal cycling, and PUND waveforms used to measure endurance and FE polarization of the fabricated FE stacks, (b) evolution of remanent polarization ($2P_r$) over number of bipolar cycling at a high electric field of 4 MV cm^{-1}, polarization-electric field (P–E) loops for (c) pristine device and (d) after 10^4 times of cycling.

less significant m(−111) as evidenced by the shouldered peak at 31.5° and 28.5°, respectively. This means that for the superlattices the overall concentration of the FE o-phase is lower than in the single-layer La:HZO film. Both La-doping and confinement of the HZO grain size vertically should have ideally prevented m-phase formation, suggesting other factors are at play here. The main difference between the superlattice HZO and the single-layer HZO stacks is the presence of Al_2O_3/HZO interfaces in the superlattice stacks. While Al_2O_3 layers prevent the HZO grains from growing vertically, different interfacial energy associated with Al_2O_3/HZO vs. TiN/HZO interface can promote the formation of the m-phase.[15] Additionally, interfacial oxygen diffusion from these Al_2O_3 layers into the HZO layers may contribute to formation of non-FE regions. Furthermore, absence of Al_2O_3/HZO interfaces can also lead to different in-plane stress development in the reference stack, along with likely different oxygen vacancy distribution. These are reflected in the lower value of in-plane tensile stress observed for the single-layer La:HZO reference stack vs. the superlattices (774 MPa vs. ∼970 MPa), suggesting they have different FE/non-FE phase compositions. This indicates that to replicate identical FE properties of single-layer La:HZO films in the superlattices, the choice of interlayer material is crucial. In our case, interlayer material that mimics HZO/TiN interface is required. Ideally, a dielectric oxide that results in comparable interfacial energy with HZO to that of TiN with HZO, should be used as the thin interlayer.

Conclusion

In conclusion, we have demonstrated that it is possible to scale up the thickness of FE stacks using La-doped HZO-based superlattices, while preserving almost identical FE properties across them. All the superlattices post-annealing (PMA), showed similar pristine $2P_r$ value, in-plane stack stress, and o(111)/t(101) GI-XRD peak position, suggesting they have comparable FE/non-FE phase composition. More work is required to translate identical FE properties from single-layer HZO stacks to HZO superlattice stacks, which can be possibly performed by choosing appropriate interlayers that mimic the interfaces present in single-layer HZO stacks, and/or by tuning the in-plane stress in the HZO layers. Such future studies can help in developing thicker superlattice stacks that can mimic the FE properties of single thin HZO layers, enabling a way for characterizing material properties that are rather limited or challenging in the case of thin HZO layers; or in preserving identical FE properties for applications that require thick HZO films.

Author contributions

G. De: conceptualization, investigation, data curation, formal analysis, writing –original draft, and writing – review & editing. M.I. Popovici: conceptualization, investigation, validation, supervision, and writing – review & editing. S. Mukherjee: investigation, data curation, formal analysis, and writing – review & editing. D.S. Kwon: data curation, formal analysis, and writing – review & editing. F. Luciano: investigation, data curation, and writing – review & editing. T. Murphy: investigation, data curation, and writing – review & editing. G.S. Kar: resources, validation, and writing – review & editing. A. Delabie: conceptualization, validation, supervision, and writing – review & editing. J. Van Houdt: conceptualization, validation, supervision, and writing – review & editing.

Data availability

Data supporting this article is already part of figures provided. Additional data regarding X-ray reflectivity spectra has been provided in ESI.†

Conflicts of interest

There are no conflicts to declare.

Acknowledgements

References

1 T. S. Böscke, J. Müller, D. Bräuhaus, U. Schröder and U. Böttger, Appl. Phys. Lett., 2011, 99, 102903.

2 N. Ramaswamy, A. Calderoni, J. Zahurak, G. Servalli, A. Chavan, S. Chhajed, M. Balakrishnan, M. Fischer, M. Hollander, D. P. Ettisserry, A. Liao, K. Karda, M. Jerry, M. Mariani, A. Visconti, B. R. Cook, D. Mills, A. Torsi, C. Mouli, E. Byers, M. Helm, S. Pawlowski, S. Shiratake and N. Chandrasekaran, 2023 International Electron Devices Meeting (IEDM), 2023, 1–4.

3 F. Huang, B. Saini, L. Wan, H. Lu, X. He, S. Qin, W. Tsai, A. Gruverman, A. C. Meng, H.-S. P. Wong, P. C. McIntyre and S. S. Wong, 2023 IEEE Symposium on VLSI Technology and Circuits, 2023, 1–2.

4 J. Müller, T. S. Böscke, S. Müller, E. Yurchuk, P. Polakowski, J. Paul, D. Martin, T. Schenk, K. Khullar, A. Kersch, W. Weinreich, S. Riedel, K. Seidel, A. Kumar, T. M. Arruda, S. V. Kalinin, T. Schlösser, R. Boschke, R. van Bentum, U. Schröder and T. Mikolajick, 2013 IEEE International Electron Devices Meeting (IEDM), 2013, 10.8.1–10.8.4.

5 S. S. Cheema, D. Kwon, N. Shanker, R. Dos Reis, S.-L. Hsu, J. Xiao, H. Zhang, R. Wagner, A. Datar and M. R. McCarter, Nature, 2020, 580, 478–482.

6 X. Sang, E. D. Grimley, T. Schenk, U. Schroeder and J. M. LeBeau, *Appl. Phys. Lett.*, 2015, **106**, 162905.

7 M. I. Popovici, A. M. Walke, J. Bizindavyi, J. Meersschaut, K. Banerjee, G. Potoms, K. Katcko, G. V. D. Bosch, R. Delhougne, G. S. Kar and J. V. Houdt, *ACS Appl. Electron. Mater.*, 2022, **4**, 1823–1831.

8 M. I. Popovici, J. Bizindavyi, P. Favia, S. Clima, M. N. K. Alam, R. K. Ramachandran, A. M. Walke, U. Celano, A. Leonhardt, S. Mukherjee, O. Richard, A. Illiberi, M. Givens, R. Delhougne, J. V. Houdt and G. S. Kar, 2022 IEEE International Electron Devices Meeting (IEDM), 2022, 6.4.1.–6.4.4.

9 C. Künneth, R. Materlik and A. Kersch, *J. Appl. Phys.*, 2017, **121**, 205304.

10 S. Estandia, N. Dix, J. Gazquez, I. Fina, J. Lyu, M. F. Chisholm, J. Fontcuberta and F. Sánchez, *ACS Appl. Electron. Mater.*, 2019, **1**(8), 1449–1457.

11 M. H. Park, Y. H. Lee, T. Mikolajick, U. Schroeder and C. S. Hwang, *Adv. Electron. Mater.*, 2019, **5**(3), 1800522.

12 Y. Goh, J. Hwang, Y. Lee, M. Kim and S. Jeon, *Appl. Phys. Lett.*, 2020, **117**, 242901.

13 G. Segantini, B. Manchon, I. C. Infante, M. Bugnet, R. Barhoumi, S. Nirantar, E. Mayes, P. R. Romeo, N. Blanchard, D. Deleruyelle, S. Sriram and B. Vilquin, *Adv. Electron. Mater.*, 2023, **9**, 2300171.

14 Y. Yun, P. Buragohain, M. Li, Z. Ahmadi, Y. Zhang, X. Li, H. Wang, J. Li, P. Lu, L. Tao, H. Wang, J. E. Shield, E. Y. Tsymbal, A. Gruverman and X. Xu, *Nat. Mater.*, 2022, **21**, 903–909.

15 M. H. Park, Y. H. Lee, H. J. Kim, T. Schenk, W. Lee, K. D. Kim, F. P. G. Fengler, T. Mikolajick, U. Schroeder and C. S. Hwang, *Nanoscale*, 2017, **9**, 9973–9986.

16 M. A. Sahiner, R. J. V. Valk, J. Steier, J. Savastano, S. Kelty, B. Ravel, J. C. Woicik, Y. Ogawa, K. Schmidt, E. A. Cartier, J. L. J-Sweet, C. Lavoie and M. M. Frank, *Appl. Phys. Lett.*, 2021, **118**, 092903.

17 M. Lederer, T. Kampfe, R. Olivo, D. Lehninger, C. Mart, S. Kirbach, T. Ali, P. Polakowski, L. Roy and K. Seidel, *Appl. Phys. Lett.*, 2019, **115**, 222902.

18 T.-J. Chang, H.-Y. Chen, C.-I. Wang, H.-C. Lin, C.-F. Hsu, J.-F. Wang, C.-H. Nien, C.-S. Chang, I. P. Radu and M.-J. Chen, *Acta Mater.*, 2023, **246**, 118707.

19 U. Schroeder, R. Sachdeva, P. D. Lomenzo, B. Xu, M. Materano, T. Mikolajick and A. Kersch, *J. Appl. Phys.*, 2022, **132**, 214104.

20 T. Jõgiaas, M. Kull, H. Seemen, P. Ritslaid, K. Kukli and A. Tamm, *J. Vac. Sci. Technol., A*, 2020, **38**, 022406.

21 M. Berdova, X. Liu, C. Wiemer, A. Lamperti, G. Tallarida, E. Cianci, M. Fanciulli and S. Franssila, *J. Vac. Sci. Technol., A*, 2016, **34**, 051510.

22 T. Tharpe, X. Zheng, P. X. L. Feng and R. Tabrizian, *Adv. Eng. Mater.*, 2021, **23**, 2170047.

23 R. W. Whatmore, Q. Zhang, Z. Huang and R. A. Dorey, *Mater. Sci. Semicond. Process.*, 2002, **5**(2–3), 65–77.

24 T. Tharpe, E. Hershkovitz, F. Hakim, H. Kim and R. Tabrizian, *Nat. Electron.*, 2023, **6**(8), 599–609.

25 B. Zeng, S. Xie, S. Zhang, H. Huang, C. Ju, S. Zheng, Q. Peng, Q. Yang, Y. Zhou and M. Liao, *Acta Mater.*, 2024, **272**, 119920.

26 H. J. Kim, M. H. Park, Y. J. Kim, Y. H. Lee, W. Jeon, T. Gwon, T. Moon, K. D. Kim and C. S. Hwang, *Appl. Phys. Lett.*, 2014, **105**, 192903.

27 U. Schroeder, C. Richter, M. H. Park, T. Schenk, M. Pešić, M. Hoffmann, F. P. G. Fengler, D. Pohl, B. Rellinghaus, C. Zhou, C.-C. Chung, J. L. Jones and T. Mikolajick, *Inorg. Chem.*, 2018, **57**(5), 2752–2765.

28 R. Batra, T. D. Huan, G. A. Rossetti Jr and R. Ramprasad, *Chem. Mater.*, 2017, **29**(21), 9102–9109.

29 M. Tyunina, J. Levoska, O. Pacherova, T. Kocourek and A. Dejneka, *J. Mater. Chem. C*, 2022, **10**, 6770.

30 A. Herklotz, D. Lee, E.-J. Guo, T. L. Meyer, J. R. Petrie and H. N. Lee, *J. Phys.: Condens. Matter*, 2017, **29**, 493001.

31 Y.-K. Liang, J.-W. Lin, Y.-S. Huang, W.-C. Lin, B.-F. Young, Y.-C. Shih, C.-C. Lu, S. H. Yeong, Y.-M. Lin, P.-T. Liu, E. Y. Chang and C.-H. Lin, *ECS J. Solid State Sci. Technol.*, 2022, **11**, 053012.

32 H. N. Lee, H. M. Christen, M. F. Chisholm, C. M. Rouleau and D. H. Lowndes, *Nature*, 2005, **433**, 395–399.

33 J. M. Gregg, *J. Phys.:Condens. Matter*, 2003, **15**, V11.